

Analysis of In-cylinder Flow Field Anisotropy in IC Engine using Large Eddy Simulation

Chao He¹ · Wibke Leudesdorff¹ · Francesca di Mare² ·
Amsini Sadiki¹ · Johannes Janicka¹

Received: 26 April 2016 / Accepted: 30 March 2017 / Published online: 9 May 2017
© Springer Science+Business Media Dordrecht 2017

Abstract The objective of the analysis presented in this work is to investigate the distribution of the anisotropy invariants of the in-cylinder flow to examine the characteristics of the turbulence during an engine cycle and its interactions with the in-cylinder coherent structures. For this purpose, both the results of Large Eddy Simulations of the flow in an internal combustion engine under motored conditions and measurements obtained in the same configuration have been employed. Investigations include an analysis of the in-cylinder flow properties in the engine's cross plane by means of first and second order statistical moments. Additionally, the behaviour of the flows anisotropy tensor has been analysed. It has been observed that during the intake stroke the in-cylinder turbulence shows a rather anisotropic structure, whereas during the compression stroke it tends to be more isotropic. Furthermore, the degree of anisotropy increases again in correspondence of vortex breakdown, during which particularly high velocity fluctuations have been identified also by experimental investigation.

Keywords Anisotropy invariant mapping · Coherent structures · Internal combustion engine · Large eddy simulation

✉ Francesca di Mare
dimare@rsm.tu-darmstadt.de; dimare@ekt.tu-darmstadt.de;
francesca.dimare@dlr.de

¹ Institute of Energy and Power Plant Technology, Technische Universität Darmstadt, Jovanka-Bontschits-Straße 2, D-64287 Darmstadt, Germany

² Institute of Reactive Flows and Diagnostics, Technische Universität Darmstadt, Jovanka-Bontschits-Straße 2, D-64287 Darmstadt, Germany

Nomenclature

AIM	anisotropy invariant map	A_1, A_2	constants
BDC	bottom dead centre	C_s	Smagorinsky constant
bTDC	before top dead centre	C	correlation coefficient
CA	crank angle	I	specific internal energy
CCV	cycle-to-cycle variation	I, II, III	first, second and third invariant
CFD	computational fluid dynamics	M	ratio of resolved to total turbulent kinetic energy
CFL	Courant-Friedrichs-Lewy	N_{CA}	number of cycles
CPU	central processing unit	N_P	number of evaluation points
DES	detached eddy simulation	P, Q	cycle samples
DISI	direct injection spark ignition	Pr	Prandtl number
GDI	gasoline direct injection	R	gas constant
IC	internal combustion	S_{ij}	rate of strain
LDV	laser Doppler velocimetry	T	temperature
LES	large eddy simulation	T_0	reference temperature
PDF	probability density function	T_{ij}	viscous tensor
PIV	particle image velocimetry	W	mean molecular weight
POD	proper orthogonal decomposition	b_{ij}	normalized anisotropy tensor
QSOU	quasi-second-order upwind	c_p	constant pressure specific heat capacity
RANS	Reynolds-averaged-Navier-Stokes	c_v	constant volume specific heat capacity
rms	root mean square	e	internal energy
RSGT	Reynolds-stress gradient tensors	h	enthalpy
RSM	Reynolds stress model	k	turbulent kinetic energy
RST	Reynolds stress tensor	p	pressure
SGS	subgrid scale	q_i	energy flux
TDC	top dead centre	t	time
TPIV	tomographic particle image velocimetry	x, y, z	cartesian coordinates
URANS	unsteady Reynolds-averaged-Navier-Stokes	u, v, w	velocity components in x -, y - and z -direction
$\tilde{*}$	Favre-filtered	Δ	filter length scale
$\bar{*}$	spatially filtered/resolved	δ	Kronecker delta
$\langle * \rangle$	temporal filtered/phase averaged	θ	crank angle
$*'$	temporal fluctuation	λ	thermal conductivity
$*^{sgs}/*_{sgs}$	subgrid scale	λ_i	i -th eigenvalue of normalized anisotropy tensor
$*_{eff}$	effective	μ	dynamic viscosity
$*_{res}$	resolved	ν	kinematic viscosity
$*_{rms}$	root mean square	ρ	density
$*_s$	sensible	σ_i	i -th eigenvalue of Reynolds stress tensor
$*_t$	turbulent	τ_{ij}	Reynolds stress tensor
		τ'_{ij}	viscous tensor

1 Introduction

The evolution of the in-cylinder flow pattern in internal combustion (IC) engines has been recognized to affect combustion in gasoline as well as in diesel engines through its influence on the mixing processes [1–3]. Numerous efforts have been made in order to describe the evolution of coherent structures and turbulence in IC engines by means of numerical simulations. Reynolds-Averaged-Navier-Stokes (RANS) techniques have been applied to study the influence of piston configuration on the tumbling motion (see for example Gosman et al. [4]). Roy and Penven [5] compared the predictions of Reynolds Stress Model (RSM) with those of the classic k - ε -model. The superiority of the RSM approach at describing the vorticity and turbulent kinetic energy fields observed in the experimental configuration of Marc et al. [6] was confirmed in this study. However, intrinsically unsteady processes, like air-fuel mixing, changes of in-cylinder turbulence levels and the evolution of total kinetic energy, which lead ultimately to cycle-to-cycle variation (CCV), cannot be accurately captured by means of RANS or unsteady RANS (URANS) approaches; rather they are best investigated using scale-resolving techniques such as Large Eddy Simulation (LES).

Haworth and Jansen [7] explored in 1996 some theoretical issues related to the application of LES to the simulation of IC-engines. LES was successively applied to investigate the development of in-cylinder turbulence as it is more able to capture fine spatial and temporal flow structures and hence describe essentially unsteady, spatially anisotropic phenomena such as temperature stratification, onset of autoignition, and development of the reaction fronts in IC-engines. LES has been successfully used to examine the effects of cyclic variability on mixing and combustion processes (see for example Celik et al. [8], Goryntsev et al. [9], Enaux et al. [10], Nguyen et al. [11], among others). Further, a comparison of two different simulation approaches has been presented by Nguyen and Janas [12]. A recent review of applications of LES in IC-engines is provided by Rutland [13]. Due to the high computational costs of well-resolved LES simulations, hybrid LES/RANS methods have also been employed to analyse the evolution of the velocity field structure, although in absence of reactions. Bottone et al. [14], for instance, carried out multi-cycle simulations using LES and a hybrid LES/RANS approach and compared the predictions with both measurements and results obtained using a RANS approach, showing that LES could very accurately reproduce the experimental observations. Hasse et al. [15] also recently investigated CCV and Hartmann et al. [16] provided an analysis of the flow through the intake port of an IC engine, both using a Detached Eddy Simulation (DES).

Nowadays efforts are being made to generate and provide comprehensive experimental database for in-cylinder flow analysis (Borée et al. [17], Spessa [18], Baum et al. [19, 20]). Measurements are carried out essentially in optical engines and generic laboratory configurations. Earlier measurements applied Laser Doppler Velocimetry (LDV) and Particle Image Velocimetry (PIV) to describe the way flow structures are generated and modified throughout the cylinder during the cyclic piston motion [6]. Recently planar PIV and tomographic PIV (TPIV) were utilized by Zentgraf et al. [21, 22] (and therein quoted contributions) to analyse the turbulent in-cylinder flow field in optical engine configurations, and thus provide an extensive velocimetry database which lend itself to a detailed statistical analysis of fundamental turbulent quantities. Among these the local distribution of the Reynolds-stress gradient tensors (RSGT) were found to be particularly relevant wherefore the anisotropic Reynolds-stress invariants were employed to characterize the structure of the turbulence in the in-cylinder flow over several crank angles (CA) and engine speeds under common spark ignition engine operations. Vernet [23] also utilized stereo-PIV measurements to study

the in-cylinder flow and to analyse turbulence anisotropy. Advanced post-processing techniques, such as Proper Orthogonal Decomposition (POD) have been applied to experimental as well as numerical datasets and provided interesting insight in the behaviour and topology of the in-cylinder flows [24–28].

Borée et al. [17] described the structure typically observed in both spark ignition and compression ignition engines. In particular they reviewed various approaches to the characterization of the flow topology, examined and described the turbulence evolution and related turbulence scales to engine parameters (bore, stroke, speed, etc.). Recently, Baum et al. [19] used the Q-criterion to reveal and analyse coherent structures in SI engines.

It has been shown by experimental investigations that the degree of anisotropy represents an important characteristic of the in-cylinder flow field, since typical engine flows are highly anisotropic and intrinsically unsteady [18, 21]. According to Lumley and Newman [29] the level of turbulence anisotropy can be isolated from all other flow properties and quantified using the anisotropy tensor (non-dimensional traceless deviatoric part of the Reynolds stress tensor (RST)) and its scalar invariants. Plotting the second invariant as function of the third one results in the so called anisotropy invariant map (AIM) [29]. According to Lumley [30] all realizable turbulence must lie within the AIM whilst boundaries of the map characterize special states of turbulence. Using the AIM as a tool to describe the state of the turbulence, Lee and Reynolds [31] related different shapes of the stress field to the value of the invariants such as *rod*- and *disk*- like turbulence. However, in their description Lee and Reynolds were focusing on the turbulent eddies rather than on the stress field itself as pointed out by Simonsen and Krogstad [32]. The latter described the fundamental relationships existing between the shape of the stress tensor and its invariants, and performed a continuum-mechanics-based analysis to clarify and unify the terminology.

A comprehensive anisotropy analysis can be subject to a statistical interpretation and thus complement classical statistical methods due to the low complexity of the data representation. The illustration of the evolution of the turbulence and of the total kinetic energy during the engine cycle can help gaining a deeper understanding of the mechanisms involved in the appearance of CCV. Since attempts were made to determine the occurrence of CCV at specific moments of the engine cycle (see for example Voisine et al. [33]), it could be possible to seek also connections between the occurrence of CCV and the anisotropic behaviour of the in-cylinder flow.

Previously, attempts at characterizing the turbulent flow field anisotropy have been conducted in simplified configurations and from a strictly theoretical viewpoint [34–39]. Recently, however, Zentgraf et al. [21, 22] have provided experimental data on anisotropy in a motored 4-stroke, single-cylinder research engine. The configuration is ideally suited for a detailed comparison with numerical predictions obtained by means of LES. In this work the flow field predicted by LES computations of the same configuration measured in [21] and [22] will be analysed with respect to the structure of the anisotropy tensor; results will be compared with those obtained by Zentgraf et al. [21, 22] applying the same post-processing technique (AIM) to both numerical and experimental datasets.

In the following sections a description of the problem formulation, including the mathematical models and the anisotropy invariant mapping will be provided. The experimental and numerical setup as well as the data processing technique is described in Section 3. Finally the results will be discussed in Section 4. In particular, the experimental data reported by Baum et al. [19], Zentgraf et al. [21, 22] will be first compared to the numerical predictions in a classic statistical sense, and a detailed analysis of the anisotropy properties of the flow will be discussed.

2 Problem Formulation

In order to provide deeper insight into the nature of turbulence within IC engines, turbulence structures and anisotropy evolution are investigated in this paper using the invariant technique proposed by Lumley and Newman [29] and Lumley [30]. This technique is based on the definition of the AIM, where the state of the turbulence is specified by the second and third invariant of the normalized anisotropy tensor. Thus the development of the turbulence can be examined and illustrated in different regions of an IC engine.

In the following sections mathematical formulations and basic principles regarding numerical computation and anisotropy invariant mapping are presented.

2.1 Mathematical model

The mathematical model consists of the Favre-filtered conservation equations for mass, momentum and energy (Eq. 1–3), completed by the appropriate constitutive and state relations [2, 3]. The filtering is performed implicitly by using the LES mesh as filter width. The Favre-filtered quantities are marked by the tilde operator and the LES-filtered by the over-bar operator. Terms due to chemistry and spray can be neglected, as motored conditions are considered.

Conservation of mass:

$$\frac{\partial \bar{\rho}}{\partial t} + \frac{\partial (\bar{\rho} \tilde{u}_j)}{\partial x_j} = 0 \tag{1}$$

Conservation of momentum:

$$\frac{\partial (\bar{\rho} \tilde{u}_i)}{\partial t} + \frac{\partial (\bar{\rho} \tilde{u}_i \tilde{u}_j)}{\partial x_j} = \frac{\partial}{\partial x_j} \left[\bar{\tau}'_{ij} - \bar{\rho} (u_i \tilde{u}_j - \tilde{u}_i \tilde{u}_j) \right] - \frac{\partial \bar{p}}{\partial x_i} \tag{2}$$

Conservation of internal energy:

$$\frac{\partial (\bar{\rho} \tilde{e})}{\partial t} + \frac{\partial (\bar{\rho} \tilde{u}_j \tilde{e})}{\partial x_j} = -\bar{p} \frac{\partial \tilde{u}_j}{\partial x_j} + \bar{\tau}'_{ij} \frac{\partial \tilde{u}_i}{\partial x_j} + \frac{\partial}{\partial x_j} \left[\bar{\lambda} \frac{\partial \tilde{T}}{\partial x_j} - \bar{\rho} (u_i \tilde{e} - \tilde{u}_j \tilde{e}) \right] \tag{3}$$

The following constitutive and state relations hold:

$$\bar{\tau}'_{ij} = 2\mu \left(\tilde{S}_{ij} - \frac{1}{3} \tilde{S}_{kk} \delta_{ij} \right) \tag{4}$$

$$\tilde{S}_{ij} = \frac{1}{2} \left(\frac{\partial \tilde{u}_i}{\partial x_j} + \frac{\partial \tilde{u}_j}{\partial x_i} \right) \tag{5}$$

$$\mu = \frac{A_1 T^{3/2}}{T + A_2}$$

where $A_1 = 110 \text{ K}$ and $A_2 = 1.457 \times 10^{-6} \frac{\text{kg}}{\text{ms}\sqrt{\text{K}}}$ (6)

$$\bar{p} = \bar{\rho} \frac{R}{W} \tilde{T} \text{ with } R = 8.314 \frac{\text{J}}{\text{mol} \cdot \text{K}} \tag{7}$$

$$c_p - c_v = \frac{R}{W} \tag{8}$$

The subgrid-scale fluctuations of both the molecular viscosity in Eq. 4 and of the gas constant in Eq. 7 have been neglected.

The internal energy e in Eq. 3 is defined as following; hence the filtering operator has been omitted in the notation:

$$e = h - \frac{p}{\rho} = e_0 + \int_{T_0}^T c_v dT - \frac{p}{\rho}, \text{ with } h = h_0 + \int_{T_0}^T c_p dT \tag{9}$$

Where h_0 and e_0 are the formation enthalpy and energy, respectively, at $T = T_0$. The constant volume specific heat is calculated from the internal energy:

$$c_v = \left. \frac{\partial e}{\partial T} \right|_v \tag{10}$$

The filtering operation gives rise to unclosed terms in the momentum and energy equations which require closure:

$$\tau_{ij}^{sgs} = u_i \tilde{u}_j - \tilde{u}_i \tilde{u}_j \text{ and } q_j^{sgs} = \tilde{u}_j e - \tilde{u}_j \tilde{e} \tag{11}$$

The unresolved momentum flux can be divided into an isotropic and an anisotropic part, whereas the isotropic part is included into the modified pressure. The anisotropic part of the subgrid scale (SGS) stresses τ_{ij}^{sgs} (left side of Eq. 12) is modelled according the Boussinesq approximation (see [37]):

$$\tau_{ij}^{sgs} - \frac{\delta_{ij}}{3} \tau_{kk}^{sgs} = -2\nu_t \left(\tilde{S}_{ij} - \frac{\delta_{ij}}{3} \tilde{S}_{kk} \right) \tag{12}$$

where \tilde{S} is the filtered rate of strain. The turbulent kinematic viscosity is modelled using the classical Smagorinsky model [40] with a Smagorinsky constant set to C_S of 0.1 (see Eq. 13). The filter width Δ in this expression is determined as $\Delta = (\Delta x \Delta y \Delta z)^{1/3}$.

$$\nu_t = (C_S \Delta)^2 |\tilde{S}|, \text{ with } |\tilde{S}| = \sqrt{2\tilde{S}_{ij}\tilde{S}_{ij}} \text{ and } \nu_t = \frac{\mu_t}{\tilde{\rho}} \tag{13}$$

The subgrid fluxes in the energy equation q_j^{sgs} are closed using a gradient approach with the turbulent Prandtl number Pr_t set equal to 0.7:

$$q_j^{sgs} = -\frac{\mu_t}{Pr_t} \frac{\partial \tilde{e}}{\partial x_j} \tag{14}$$

As shown in the literature [41], the contribution of the pressure-dilatation term to the SGS thermal fluxes in flows at low Mach-numbers (0.3 - 0.6) is indeed negligible and it has been therefore simply ignored. Based on similar arguments, the contributions of the small scale fluctuations to the viscous dissipation are also neglected; this justifies the formulation presented in Eq. 2.

2.2 Anisotropy invariant mapping

The RST stems from momentum transfer by the fluctuating (resolved) velocity field and thus contains information about the relative strengths of different velocity fluctuation components, which provide information about the *componentality* [42–44] of the turbulence.

In simulations of IC-engine flows phase-averaging at particular crank angles is especially well suited for a statistical characterisation of the velocity and turbulence field, as it will be shown in Section 3.3. In the following, overbars and tilde to designate filtered (resolved) quantities will be omitted to simplify the notation unless otherwise specified and the symbol τ_{ij} is intended to be referred to the *resolved* Reynolds stresses.

The resolved Reynolds stress tensor can be decomposed in its isotropic and deviatoric parts which read:

$$\tau_{ij} = \tau_{ij}^I + \tau_{ij}^A, \text{ with } \tau_{ij}^I = \frac{1}{3} \tau_{kk} \delta_{ij} \text{ and } \tau_{ij}^A = \tau_{ij} - \frac{1}{3} \tau_{kk} \delta_{ij} \tag{15}$$

Only the anisotropy tensor τ_{ij}^A is effective in transporting momentum [37]. Its normalized form b_{ij} can be defined starting from Eq. 16. The symmetry of the RST implies that the traceless tensor b_{ij} , which vanishes in isotropic turbulence, is also symmetric ($b_{ij} = b_{ji}$):

$$b_{ij} = \frac{\tau_{ij}^A}{\tau_{kk}} = \frac{\tau_{ij}}{\tau_{kk}} - \frac{1}{3} \delta_{ij} \tag{16}$$

By replacing the expression for the resolved turbulent kinetic energy $k_{res} = \frac{1}{2} \langle u'_i u'_i \rangle$ in (16) this becomes:

$$b_{ij} = \frac{\langle u'_i u'_j \rangle}{2k_{res}} - \frac{\delta_{ij}}{3} \tag{17}$$

From (17) it can be seen that the values attainable by b_{ij} are restricted to the intervals $-1/3 < b_{ij} < 2/3$ for $i = j$ and to $-1/2 < b_{ij} < 1/2$ for $i \neq j$ [42].

The eigenvalues and the related eigenvectors of the anisotropy tensor can be determined by evaluating the characteristic Eq. 18:

$$\lambda^3 - I\lambda^2 + II\lambda - III = 0 \tag{18}$$

where I, II and III are respectively its first, second and third invariant. By definition, invariants are scalars obtained from a tensor, which are independent of the coordinate system and therefore have the same values in any coordinate system (see Lumley [45]).

Considering the symmetric, second-order tensor b_{ij} (with corresponding matrix \mathbf{B}) three principal invariants can be defined, which are linearly independent:

$$\begin{aligned} I &= \text{tr}(\mathbf{B}) = b_{ii} \\ II &= \frac{1}{2} \left\{ [\text{tr}(\mathbf{B})]^2 - \text{tr}(\mathbf{B}^2) \right\} = \frac{1}{2} \left[(b_{ii})^2 - b_{ij}^2 \right] \\ III &= \det(\mathbf{B}) = \frac{1}{6} (b_{ii})^3 - \frac{1}{2} b_{ii} b_{jj}^2 + \frac{1}{3} b_{ii}^3 \end{aligned} \tag{19}$$

As the anisotropy tensor is traceless by definition, the first invariant $I = b_{ii}$ vanishes, such that the anisotropic Reynolds stresses can be characterized by just two linearly independent invariants, the principal invariants II and III .

Remembering that $b_{ii} = 0$, $b_{ii}^2 = b_{ij} b_{ji}$ and $b_{ii}^3 = b_{ij} b_{jk} b_{ki}$, the expressions for II and III can be thus simplified:

$$II = -\frac{1}{2} b_{ij} b_{ji} \text{ and } III = \frac{1}{3} b_{ij} b_{jk} b_{ki} \tag{20}$$

Several definitions of the anisotropy tensor invariants can be found in the literature. Eq. 20, which will be used throughout this work, corresponds to the formulation proposed by Lumley [30], which differs only by a simple factor from the ones suggested by Lumley

and Newman [29]. Choi and Lumley [46] proposed a coordinate transformation to examine the nonlinear behaviour during the return to isotropy of homogeneous turbulence. As invariants are the same in every coordinate system, they can be evaluated in a system having as basis the tensor's principal axes too, using its coordinate-independent eigenvalues λ_i . In general, the anisotropy tensor invariants are non-linear functions of stresses (see Eq. 20 and [29, 30] and [46]); however an equivalent linear representation of the anisotropy invariants (see for example Radenković [38], Banerjee et al. [42] or Emory and Iaccarino [43]) can also be adopted to obtain an invariant mapping.

The analysis of the second and third invariant can provide a way of quantifying anisotropy in a turbulent flow, independently of the chosen coordinate axis. To further define the dependency between the relative sizes of the principal normal Reynolds stresses and the invariants of the anisotropy tensor, Simonsen and Krogstad [32] as well as Banerjee et al. [42] introduced a relationship between the eigenvalues σ_i of the RST τ_{ij} and the eigenvalues λ_i of the anisotropy tensor b_{ij} , based on the principle of eigenvalue decomposition [37]:

$$\lambda_i = \frac{\sigma_i}{2k_{res}} - \frac{1}{3} \quad (21)$$

From these eigenvalues the turbulence componentality can be determined. Turbulent states, defined as *one-, two- or three-component turbulence* can be identified depending on the number of non-zero eigenvalues of the RST ($\sigma_i \neq 0$), which represent the velocity fluctuations transformed into principal axis. Referring to relationship (21) this means $\lambda_i \neq -1/3$. In the case of *isotropic* turbulence the three eigenvalues are obviously equal. If only two eigenvalues are equal in magnitude, the state is referred to as *axisymmetric turbulence*. *Anisotropic turbulence* is occurring if all eigenvalues are of different magnitude. The special state realised when at least one eigenvalue vanishes is referred to as *plane-strain*.

A characterization of the stress field, defined by the three principal Reynolds stresses can be achieved analysing the properties of its secular (canonical) form, which describes a surface in the three-dimensional space having as basis the principal turbulent stresses. Based on the earlier work of Lumley and Newman [29] and Lumley [30], Choi and Lumley [46] reported, that the shape of the RST can be specified by a spheroidal structure, the energy ellipsoid, the radii of which correspond to the eigenvalues λ_i of the anisotropy tensor. Assuming a spherical shape for isotropic turbulence, the shape of the stress tensor changes to an oblate spheroid shape (also called *pancake-shaped*) in case of axisymmetric contraction and to a prolate shape (also called *cigar-shaped*) in case of axisymmetric expansion, which was also pointed out and illustrated by Simons and Krogstad [32], Hamilton and Cal [47] and Uruba [48]. According to their work, a summary of the states of the turbulence along with the corresponding shape of the energy ellipsoid and the eigenvalues of the anisotropy tensor is given in Table 1 and in Fig. 1.

Some confusion, as can be also evinced from the literature, can arise by the description of turbulent structures, depending on whether the shape of the stress tensor or the nature of vertical structure is considered (see for example Simons and Krogstad [32]). In this work the classification of the turbulence is based on the eigenvalues of the RST and therefore on the shape of the energy ellipsoid.

3 Analysis

In the following sections, the experimental and numerical setup will be presented along with the data processing technique adopted.

Table 1 Characteristics of RST and anisotropy tensor

State of turbulence	Shape of spheroid	Invariants	Eigenvalues of b_{ij}
Isotropic	sphere	$II = III = 0$	$\lambda_i = 0$
One-component	line	$II = 2/27, III = -1/3$	$\lambda_1 = 2/3, \lambda_2 = \lambda_3 = -1/3$
Two-component, axisymmetric	disk	$II = 1/108, III = -1/12$	$\lambda_1 = \lambda_3 = 1/6, \lambda_2 = -1/3$
Two-component	ellipse	$III = -(1/27+III/3)$	$\lambda_1 + \lambda_3 = 1/3, \lambda_2 = -1/3$
Axisymmetric (one small λ) ($III < 0$)	Oblate spheroid	$III = -2(-III/3)^{3/2}$	$-1/3 < \lambda_2 < 0, 0 < \lambda_1 = \lambda_3 < 1/6$
Axisymmetric (one large λ) ($III > 0$)	Prolate spheroid	$III = 2(-III/3)^{3/2}$	$0 < \lambda_1 < 1/3, -1/6 < \lambda_2 = \lambda_3 < 0$

3.1 Experimental setup

The configuration investigated in this work is located at Technische Universität Darmstadt and is part of the “Darmstadt engine workshop” (<http://www.rsm.tu-darmstadt.de>) [19, 20]. It is a 4-stroke single-cylinder direct injection spark ignition (DISI) engine with four canted valves and a pentroof cylinder head. The combustion chamber is optically accessible by means of a quartz-glass cylinder and a flat quartz-glass piston-crown window. A Gasoline Direct Injection (GDI) system is available where the fuel-injector is mounted at the side between the intake valves. The spark plug however is positioned in the centre of the cylinder head. In the present study only motored conditions are considered, wherefore the spark plug was removed and replaced by a threaded plug and the injector is inactive during the measurements. Further engine details and operating parameters are listed in Table 2.

To validate the results of the simulations, a comparison with experimental data was performed. Therefore, the flow field data obtained by planar PIV and TPIV measurements at the symmetry plane ($y = 0$ mm) were used. The volumetric flow was resolved within a $47 \times 35 \times 8$ mm³ volume, corresponding to the planar PIV measurement interrogation window. The final interrogation size was $64 \times 64 \times 64$ pixel and the spatial resolution in the TPIV measurements was 1.76 mm. A detailed description of the measurement techniques can be

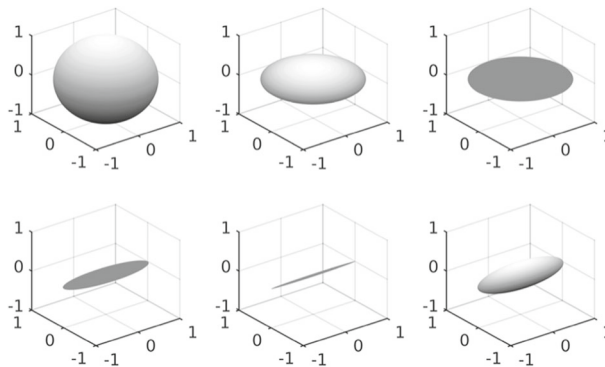


Fig. 1 Shapes of energy spheroid; top row shows sphere, oblate spheroid and disk, bottom row shows ellipse, line and prolate spheroid

Table 2 Geometrical parameters and operation parameters

	Value	Unit
Bore	86	mm
Stroke	86	mm
Connecting rod length	148	mm
Max. valve lift	9.5	mm
Cylinder clearance height	2.6	mm
Compression ratio	8.5	–
Engine speed	800	rpm
Intake mean pressure	0.95	bar
Intake mean temperature	295	K
Exhaust mean pressure	1.003	bar
Exhaust mean temperature	317	K
Intake valve open time (IVO)	325	° CA aTDC
Intake valve close time (IVC)	125	° CA bTDC
Exhaust valve open time (EVO)	105	° CA aTDC
Exhaust valve close time (EVC)	345	° CA bTDC

found in Baum et al. [19]. The experimental data was obtained during intake stroke at 270° CA before top dead centre (bTDC) and compression stroke at 90° CA bTDC. For the phase-averaged velocity field obtained by PIV measurements 600 cycles were used and in terms of TPIV measurements 300 cycles were used. Top dead centre (TDC) during the working cycle correspond to 0° CA, wherefore negative CA values in the following figures indicate

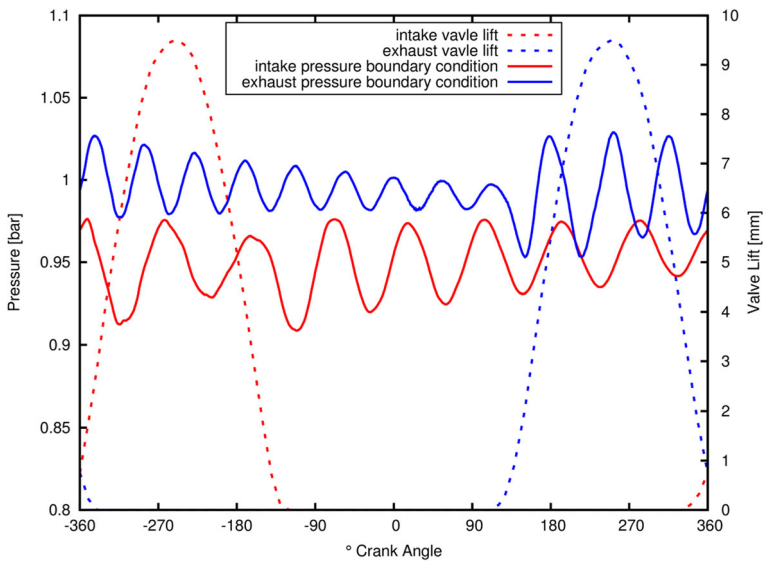


Fig. 2 Pressure boundary condition (continuous) and valve lift (*dashed*) for intake (*red*) and exhaust (*blue*) valve

the period before TDC. The valve lift for this research engine is illustrated in Fig. 2 (dashed lines). A comprehensive description of the experimental setup and the operating details can be found in Baum et al. [20].

3.2 Numerical setup

The numerical simulation of in-cylinder flow was performed using the computational fluid dynamics (CFD) code KIVA-4mpi, developed at Los Alamos National Laboratory [49].

The governing equation described in Section 2.1 are discretised on a moving mesh according to the ALE approach, see Torres and Trujillo [50] or Torres et al. [51]. The temporal discretization scheme used is the first-order implicit Euler. For the spatial discretization a quasi-second-order upwind (QSOU) scheme is used [49]. The time step is adjusted during the computation to fulfil accuracy requirements, conditioned on the given maximum mesh movement per time step and the magnitude of the strain rate and the Courant-Friedrichs-Lewy (CFL) parameter remains smaller than 1. Variables are stored according to a staggered arrangement.

Two structured meshes consisting of hexahedral elements [52] with different resolution were used to discretise the complete geometry of the IC engine including intake and exhaust. The average cell width, (taken as the filter width and defined in Section 2.1), varied within the engine geometry; in the coarse mesh, this was approximately equal to 0.6 mm around the intake valve and 0.8 mm in the body of the cylinder. At TDC the engine geometry contains around 0.26 million cells, at bottom dead centre (BDC) around 1.2 million cells. The fine mesh consists of 0.41 million cells at TDC and of 1.76 million cells at BDC. The mean cell width was approximately 0.4 mm around the intake valves and 0.72 mm in the cylinder body. For visualization purposes, the computational domain during compression at 90° CA bTDC is shown in Fig. 3 (left).

In general, 12 CPUs (central processing unit) were used to compute the cycles as will be described in Section 3.3. Considering this, approximately 56.31 hours were required to calculate one cycle using the coarse mesh and approximately 78.23 hours to calculate one cycle using the fine mesh.

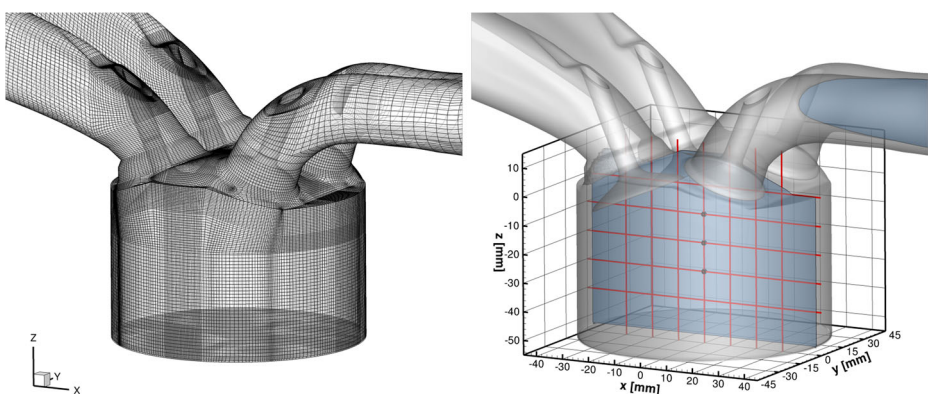


Fig. 3 Mesh at 90° CA bTDC (left) and illustration of analysis planes (right), where statistical evaluation is carried out along the z-axis and along the x-axis at $y = 0$ (red lines). Black points are marking the stationary points evaluated in Fig. 18

The initial temperature and pressure in the intake and exhaust duct was set to the experimentally determined averaged values, see Table 2. The time-dependent pressure boundary conditions for the inlet and the exhaust at every CA were also obtained from measured pressure and are displayed in Fig. 2 (continuous lines) (see Baum et al. [20]). In general, the in-cylinder mean pressure profile and the trapped mass were very well reproduced (see Fig. 4). At the walls simple no-slip conditions were assumed with no special treatment. The implications of this choice, bound to the simulation tool adopted, will be discussed further in the following sections. A marginally better treatment could be the use of wall laws (see for example [53, 54]) although the departure from equilibrium conditions in the wall layer and the fact that a logarithmic expansion is strictly valid only in the mean would render such a treatment is also debatable [53, 54].

3.3 Data processing

To define a turbulent flow field, statistical methods were applied, which make use of the Reynolds decomposition. Here, an instantaneous variable is expressed as the sum of the mean value and a corresponding fluctuation around that mean value. This method can be employed in a stationary case. But as an IC engine configuration is the object of research, the statistical analysis becomes more complicated since the flow pattern and the investigated geometry change during one engine cycle. Taking several engine cycles into account, the in-cylinder flow can be considered quasi-periodic and a phase-averaged approach can be used for the decomposition [55]. By averaging the instantaneous velocity $U(\theta, n)$ at a specific CA position θ and cycle n over the whole number of cycles N_{CA} considered, one can obtain the phase-averaged velocity $\langle U(\theta) \rangle$ at this CA (see Eq. 22). By subtracting the phase-averaged velocity from the instantaneous velocity at a certain CA position, one can obtain the fluctuating part $U'(\theta, n)$ around the phase-averaged velocity, presented by Eq. 23. Additionally to the phase-averaged velocity, which is a moment of first order, the root mean square (rms) velocity U_{rms} , a moment of second order, can be used to describe the flow field and can be determined using expression (24).

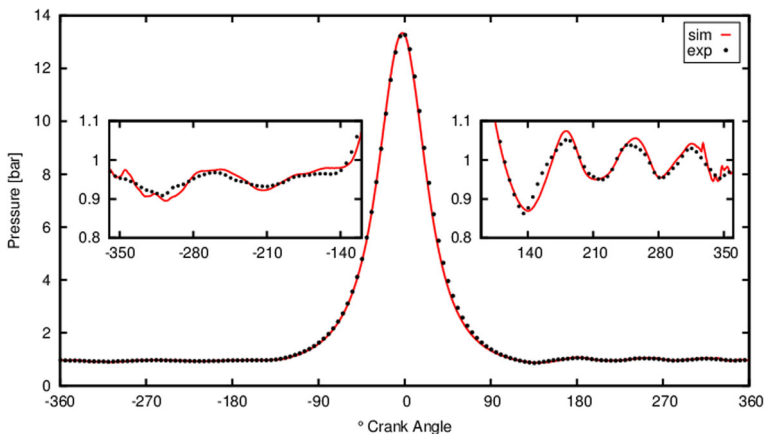


Fig. 4 In-cylinder pressure including detailed view. Comparison between experiments (*black points*) and simulation with a fine mesh (*red line*)

It should be mentioned here, that there is an ongoing debate in the literature whether the CCV in the individual cycle mean can be considered as part of turbulence (see for example [8, 55–57]). In this work, the fluctuating velocity component arising from the phase-averaging procedure combines both high- and low-frequency fluctuations, wherefore there is no differentiation being made between CCV and turbulence in the classical sense.

$$\langle U(\theta) \rangle = \frac{1}{N_{CA}} \sum_{n=1, N_{CA}} U(\theta, n) \tag{22}$$

$$U(\theta, n) = \langle U(\theta) \rangle + U'(\theta, n) \tag{23}$$

$$U_{rms}(\theta) = \sqrt{\frac{1}{N_{CA}} \sum_{n=1, N_{CA}} (U(\theta, n) - \langle U(\theta) \rangle)^2} \tag{24}$$

The amount of modelled with respect to resolved turbulent kinetic energy can be conveniently employed to assess the quality and reliability of the numerical predictions. In this work the following index (see Pope [37] and di Mare et al. [53]) has been adopted

$$M(x, t) = \frac{k_{res}(x, t)}{k_{res}(x, t) + k_{sgs}(x, t)} \tag{25}$$

While the resolved turbulent kinetic energy is given by the expression in Section 2.2 the turbulent kinetic energy of the subgrid structures is calculated according to the approach of Yoshizawa and Horiuti [58]. The quality of the LES is further discussed in Section 4.1 when presenting the in-cylinder flow field analysis.

A challenge faced by LES is the long simulation times needed for the consecutive engine cycles. According to the literature a minimum of 50 cycles are required for reliable statistics to be obtained (see for example Baumann et al. [54], Goryntsev [59] and references therein). A cycle-parallelization technique was used in this paper to reduce the computational efforts whereby multiple runs are performed in a parallel manner. In the present research three runs were started from different initial CA and different initial piston positions, respectively, each one simulating 20 consecutive cycles (see Table 3). The initial temperature and pressure for the relevant CA were set equal to the measured averaged values. A total of 60 cycles could be thus simulated with a reduction of 2/3 in computing time.

These 60 cycles can only be selected as basis for further analysis, if the fluctuations of all flow properties in each cycle are independent. In order to verify the statistical independence of the flow field realised in the parallel cycle simulations, a representative sample of points was chosen and the correlation between two cycles for two different CA (270° CA bTDC and 90° CA bTDC) was analysed using these points, uniformly distributed in the centre of the cylinder (−19 mm < x < 19 mm, −19 mm < y < 19 mm, −30 mm < z < −10 mm).

The absolute value of the correlation coefficient *C* at the selected CA θ can be calculated by means of the correlation function in Eq. 26, where *P* and *Q* indicate the sample of points at two different cycles, for example. In this expression, $P'(\theta, i)$ and $Q'(\theta, i)$ are the fluctuations of the generic flow property in cycle *P* and *Q* at CA θ and point *i*. They arise

Table 3 Initial CA and number of performed cycles for the different runs

	run1	run2	run3
Initial CA	180 bTDC	140 bTDC	100 bTDC
Performed cycles	20	20	20

from the phase-averaging procedure over the whole number of cycles, explained earlier (see Eqs. 22 and 23). By means of averaging these fluctuations over the number of sample points N_P , one can obtain the volume averaged fluctuations $\bar{P}'(\theta)$ and $\bar{Q}'(\theta)$ (see Eq. 27).

$$C(\theta) = \left| \frac{\sum_{i=1, N_P} (P'(\theta, i) - \bar{P}'(\theta)) \cdot (Q'(\theta, i) - \bar{Q}'(\theta))}{\sqrt{\sum_{i=1, N_P} (P'(\theta, i) - \bar{P}'(\theta))^2 \cdot \sum_{i=1, N_P} (Q'(\theta, i) - \bar{Q}'(\theta))^2}} \right|, \text{ with } N_P = 33600 \tag{26}$$

$$\bar{P}'(\theta) = \frac{\sum_{i=1, N_P} P'(\theta, i)}{N_P}, \quad \bar{Q}'(\theta) = \frac{\sum_{i=1, N_P} Q'(\theta, i)}{N_P} \tag{27}$$

The fluctuating flow properties of the two cycles are perfectly correlated if the coefficient is equal one, and uncorrelated if it is equal to zero. To verify the independency, the correlation coefficients were computed for each two consecutive cycles in one run as well as for each two parallel cycles in different runs. For example, in Fig. 5 the correlation coefficients of the radial velocity component fluctuation of run1 and run2 are shown, just as the correlation coefficients between those two runs. They are plotted over the cycle number, where the red and blue points show the dependency between two consecutive cycles for runs1 and run2, respectively, and the black points shows the comparisons between the cycles of run1 and run2.

The same comparison has been carried out for the other velocity component fluctuations, as well as for temperature and pressure fluctuations at 270° CA bTDC and 90° CA bTDC. Furthermore, the correlation studies between run2 and run3 as well as run1 and run3 were performed. In all comparisons a correlation coefficient smaller 0.3 was obtained, as one can observe in Fig. 5. According to literature [60] a correlation coefficient smaller 0.5 classifies the correlation as *weak*. Based on this all of the continuously simulated cycles in run1, run2 and run3 can be selected as meaningful samples, since the statistical independence of the flow property fluctuations can be assumed. For this paper, the first cycles in each run were discarded in order to reduce the effect of initial condition on the flow field, although the independency appeared already at the first simulation cycle. Finally the remaining 50 cycles (17 cycles in run1 and run2, 16 cycles in run3) were retained as samples for evaluation.

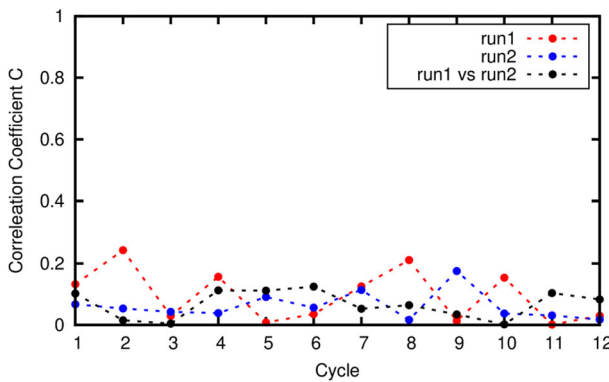


Fig. 5 Correlation of the radial velocity component fluctuations for consecutive cycles in one run (red and blue points) as well as for two parallel cycles in different runs (black points)

The phase-averaged velocity field is further analysed using the invariant map technique introduced in Section 2.2. To visualize the state of the turbulence and to display the relative evolution of the stress components, the second and third invariant of the anisotropy tensor are cross-plotted in the two-dimensional space as shown in Fig. 6, where the ordinate represents the negative second invariant $-II$ and the abscissa is the positive third invariant III . The boundaries of the so called *Lumley triangle* characterize the limiting states of the turbulence and can be described by evaluating the invariants of Eq. 20 for different cases of turbulence. The origin of the map corresponds to the three-component isotropic turbulence since both invariants II and III are zero ($b_{ij} = 0$). From here two limiting branches originate, representing two types of axisymmetric turbulence, the axisymmetric contraction represented by the red (left) boundary, and the axisymmetric expansion represented by the blue (right) boundary [46]. These lines are expressed analytically by relation (28), using the negative sign for axisymmetric contraction ($III < 0$) and the positive sign for axisymmetric expansion ($III > 0$). Along the line representing axisymmetric contraction, the third eigenvalue becomes vanishingly small as it approaches the limiting value, which represents the two-component axisymmetric state (end of the red line in Fig. 6). The same can be done in case of the axisymmetric expansion, where the two equal eigenvalues vanish as they reach the limiting value at the end of the blue line in Fig. 6, identified as the one-component state. The upper boundary line of the Lumley triangle represents two-component turbulence, and can be described using relation (29).

$$III = \pm 2 \left(-\frac{II}{3} \right)^{3/2} \tag{28}$$

$$III = - \left(\frac{1}{27} + \frac{II}{3} \right) \tag{29}$$

A summary of the boundaries described by the invariants along with the corresponding turbulence state presented in Section 2.2 is given in Table 1.

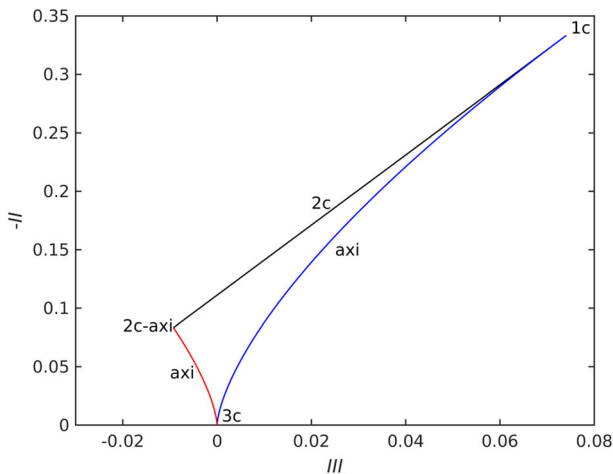


Fig. 6 AIM as a tool to quantify the degree of anisotropy; boundaries characterize limiting states of turbulence

4 Results and Discussion

In the following sections the distribution of the anisotropy invariants of the in-cylinder flow is investigated and discussed. Since a cold flow is examined, only the intake and compression stroke (360° CA bTDC till 0° CA bTDC) will be considered in this work. A classic statistical comparison of the numerical predictions and PIV as well as a detailed analysis of anisotropy distribution has been first performed at 270° CA bTDC and 90° CA bTDC: the phase averaged and rms velocity components have been collected at five different measurement stations on horizontal as well as seven different measurement stations on vertical lines throughout the cylinder as shown in Fig. 3 (right). The distribution of the second and third anisotropy invariants has been examined in both experiments (TPIV [21, 22]) and computations. Finally, the overall in-cylinder flow field anisotropy has been investigated, using averaged invariants and stationary points within the IC engine.

4.1 Flow characteristics

The phase-averaged velocity field obtained by LES during intake and compression stroke in a plane at $y = 0$ mm is displayed in Fig. 7. The displayed velocity v_{mean} is computed from the phase-averaged velocity component u and w . For a better comparison with the experimental data, the computational domain shown corresponds to the PIV interrogation window.

When focusing on the intake at 270° CA bTDC, one can observe a region of high velocity and a strongly directional flow, originating near the intake valves and extending toward the opposite cylinder wall. This jet-like flow is referred to as *intake jet* (see Baumann et al. [54]) and is a well-known phenomenon occurring in IC engines, induced by the opening of the intake valves and the downward motion of the piston. As shown in the top row of Fig. 7 both numerical simulations on the coarse as well as on the fine mesh overpredict the velocity distribution in the region of the intake jet. This observation points to a challenge faced in

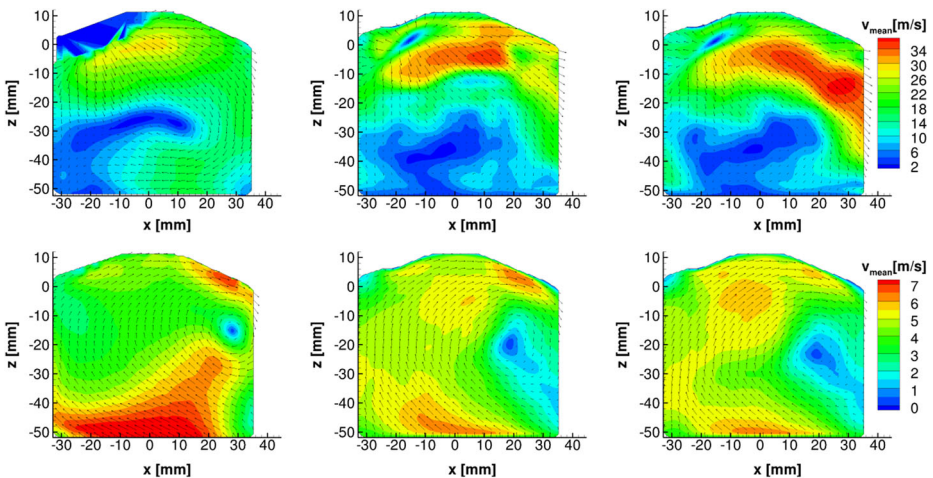


Fig. 7 Phase-averaged flow field of engine cross section during intake at 270° CA bTDC (*top*) and compression at 90° CA bTDC (*bottom*), obtained by experiment (*left*), simulation with fine mesh (*middle*) and coarse mesh (*right*)

the numerical simulation. Right after opening and before closing the valves, there are just a few cell layers located in the gap between valve and valve seat. In the worst case there is only one cell layer. This spatial resolution is relatively low, hence the velocity of high magnitude occurring at this state in the valve gap cannot be reproduced accurately, which in turn influences the profile of the intake jet. The flow in the cylinder at TDC is known to be very sensitive to the velocity at the intake valve closing (see for example Lumley [56]). During the intake stroke the formation of the (clockwise) tumble motion takes place, whose spatial position is influenced by the intake jet. The numerical simulations predict the formation of the tumble in the same region as observed in the experiments, although during compression at 90° CA bTDC a shift of the tumble centre can be observed in the predictions with respect to the measurements, as shown in Fig. 7 (bottom). Again, the deviation is stronger when considering the results obtained on the coarse mesh compared to the fine mesh. This evidence supports the hypothesis that these effects are due to the lack of accuracy in predicting the fluid motion imposed by the intake jet during the intake stroke. In the recent literature, results from different research groups can be found where higher order schemes are used and where an overall higher mesh resolution is employed (see for example [11]) or where local refinement of the mesh in critical areas is utilized to obtain better predictions (see for example [61–63]).

Phase-averaged and rms u - and w -velocity profiles, respectively along the x - and z -axis, were also evaluated at seven different positions in radial direction in the yz -plane and at five different positions along the in-cylinder axes in the xy -plane (see Fig. 3, right). During intake at 270° CA bTDC as well as during compression at 90° CA bTDC the numerical results display a good level of agreement with the experiments. In general, the computations carried out on the fine mesh reproduce, as expected, the experimental data to a higher degree of accuracy than those performed on the coarse mesh. However some deviations appear in both cases and will be discussed in the following, also based on the evidence of the quality assessment. An analysis of the LES quality was carried out to quantify the influence of the mesh size on the predictions using the quality criterion proposed by Pope [37] and described in Section 3.3. Figure 8 shows the spatial distribution of the phase averaged quality index M (see Eq. 25) at the engine cross section during intake and compression, obtained by LES with fine and coarse mesh, respectively, indicating overall a good mesh resolution in large areas of the combustion chamber. It should be mentioned, that the Pope criterion does not give a clear insight into the contribution of numerical errors. The present KIVA code is using a QSOU scheme chosen because of its numerical stability. This scheme is known to induce numerical dissipation. Further, as the walls are not well resolved, this quality index does not provide useful information here. However it is used in this work to indicate the resolution effect not close to the wall but inside the combustion chamber between the two meshes and to give an inside about the shortcomings of the mesh resolution in general.

During the intake stroke at 270° CA bTDC, the predicted phase-averaged velocity component w in the different profiles (Figs. 9 and 10) shows good agreement compared to the data obtained by the experiment. However, an increasing overprediction of the phase-averaged velocity component u within the radial positions is noticeable (Fig. 10). The same behaviour can be observed examining the profiles in Fig. 9, where the agreement between measurements and simulations degrades while moving away from the intake valves. It can be argued that the inaccuracy in predicting the characteristics of the intake jet propagates further downstream of them resulting in a displacement of the tumble motion. Applying the quality index M (see Eq. 25) it can be shown, that the mesh in this area is not fine enough to resolve at least 80% of the turbulent kinetic energy even in case of the refined grid (see Fig. 8). This is likely also to result in the underprediction of the rms values of the velocity

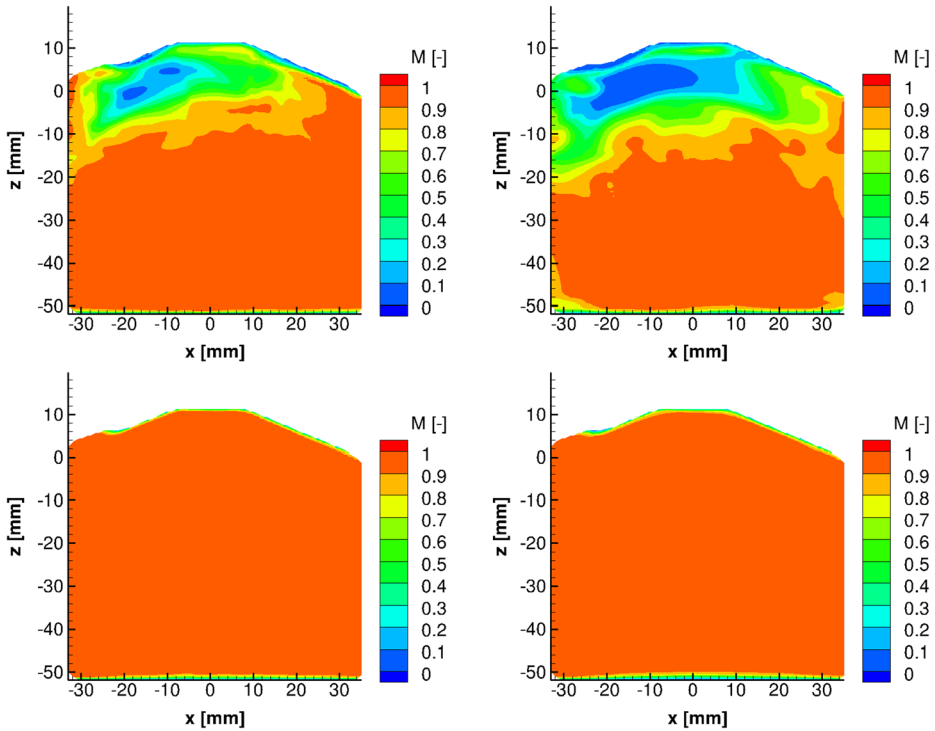


Fig. 8 Spatial distribution of phase averaged quality index M of engine cross section during intake at 270° CA bTDC (*top*) and compression at 90° CA bTDC (*bottom*), obtained by simulation with fine mesh (*left*) and coarse mesh (*right*)

components u and w in the area around the intake valves (Figs. 9 and 10). Here a higher proportion of the turbulent structure is modelled, which influences the computed flow field, as also observed in [53]. However, an improvement can be recognized when comparing the distribution of the quality index M of the two meshes during the intake stroke at 270° CA bTDC (see Fig. 8). Especially in the area around the intake valves higher values of M are indicating a better quality of the simulation carried out using the fine mesh which in turn points to the need of a higher mesh resolution in this area.

Analysing the compression stroke at 90° CA bTDC, a tendency to lower velocities and to fewer fluctuations compared to the intake stroke is noticeable. The velocity components in the profiles taken in the vertical and horizontal lines (see Figs. 11 and 12) show a good agreement with the experimental data, whereas in the axial profiles recorded further away from the cylinder's head, differences can be noticed. A discrepancy between predicted and measured rms velocity values is noticeable in the compression stroke approaching the cylinder wall (see Figs. 11 and 12). The absence of any particular treatment at the wall for both the SGS viscosity and for the turbulent stresses (damping of the SGS-viscosity and appropriate wall-law conditions) associated to the coarseness of the mesh are most likely to be the cause for this.

Finally, it is worth mentioning that the number of computed engine cycles (50) might still be insufficient to obtain converged statistics which in the experiments have been obtained

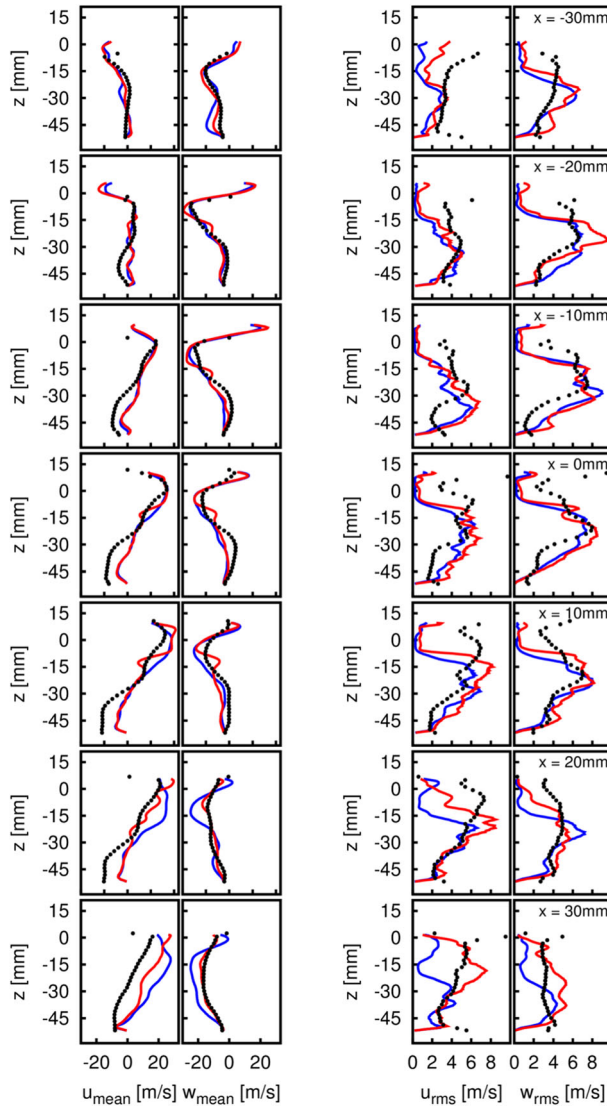


Fig. 9 Phase-averaged velocity components and corresponding rms values in z-direction during intake at 270° CA bTDC, evaluated at different radial positions (see Fig. 3, right). Comparison between experiments (black points) and LES with a coarse (blue line) and a fine (red line) mesh

using 600 and 300 cycles for PIV and TPIV measurements respectively, and that the discrepancies observed in the higher moments might improve were a higher number of cycles are computed.

4.2 Anisotropy distribution

Experimental analysis regarding the anisotropy distribution for the investigated research engine has been carried out by Zentgraf et al. [21, 22]. To display the anisotropy distribution

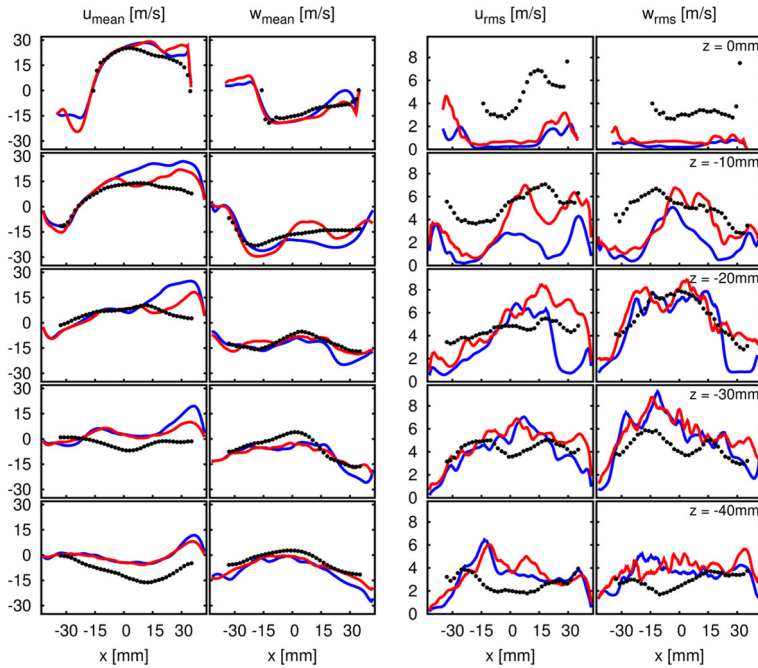


Fig. 10 Phase-averaged velocity profiles and corresponding rms values of velocity components in x-direction during intake at 270° CA bTDC, evaluated at different axial positions (see Fig. 3, right). Comparison between experiments (*black points*) and LES with a coarse (*blue line*) and a fine (*red line*) mesh

in the cross section of the engine, the local invariants for each vector were calculated and plotted within the Lumley triangle as a scatter plot. Matching the experimental analysis for comparison, the numerical results are processed as described in Section 3.3 and are presented together with experimental results in Fig. 13 for 270° CA bTDC and in Fig. 14 for 90° CA bTDC. The same number of data points and a comparable resolution in both experiment and simulation were used to obtain these data. As one can see, all data points are located inside the Lumley triangle and the majority of them at both CAs can be found near its origin. In both experimental and numerical data during intake at 270° CA bTDC, the distribution shows a broad spreading over the whole area of the Lumley triangle. However, the majority of data points are distributed in the area close to the origin, which is associated with isotropic turbulence. A careful inspection of the distributions shows that more than half of the occurrences in the experimental analysis are located in this area under a value of $-I_2 \leq 0.03$. The remaining data points are located in the region near the left and the right boarder of the Lumley triangle, where the turbulence state is rather axisymmetric i.e. two eigenvalues are dominating the third one (contraction) and one eigenvalue is dominating the other two (expansion), respectively. On the contrary, the numerical data show only 38% of the data points located beneath $-I_2 \leq 0.03$. Furthermore, considering the number of points found beneath $-I_2 \leq 0.02$ and $-I_2 \leq 0.01$, it can be observed that the experimental data show higher density in both regions. This is consistent with the deviations observed in the rms values during the intake stroke, as pointed out in Section 4.1, since the invariants are calculated by means of the RST, which represents the interactions among turbulent velocity fluctuations.

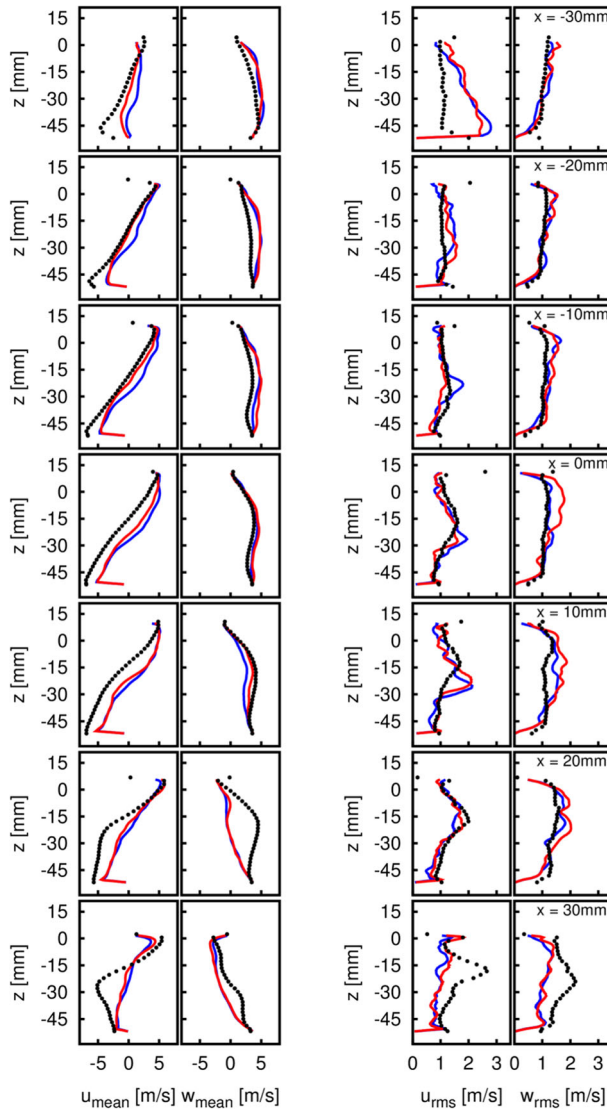


Fig. 11 Phase-averaged velocity profiles and corresponding rms values of velocity components in z -direction during intake at 90° CA bTDC, evaluated at different radial positions (see Fig. 3, right). Comparison between experiments (black points) and LES with a coarse (blue line) and a fine (red line) mesh

At 90° CA bTDC, a higher tendency towards the state of isotropic turbulence is seen compared to the intake stroke. The scatter is similar in the experimental and numerical analysis, whereas the experimental analysis shows a stronger tendency of the turbulence towards axisymmetric expansion (right boarder of the Lumley triangle) than the numerical predictions. Further, both sets of data points remain below $-I_2 \leq 0.08$ and $-I_3 \leq 0.008$. A better agreement between experimental and numerical distribution is observed comparing the amount of data points beneath $-I_2 \leq 0.02$ and $-I_2 \leq 0.01$, consistently with the analysis of the rms values at the same CA.

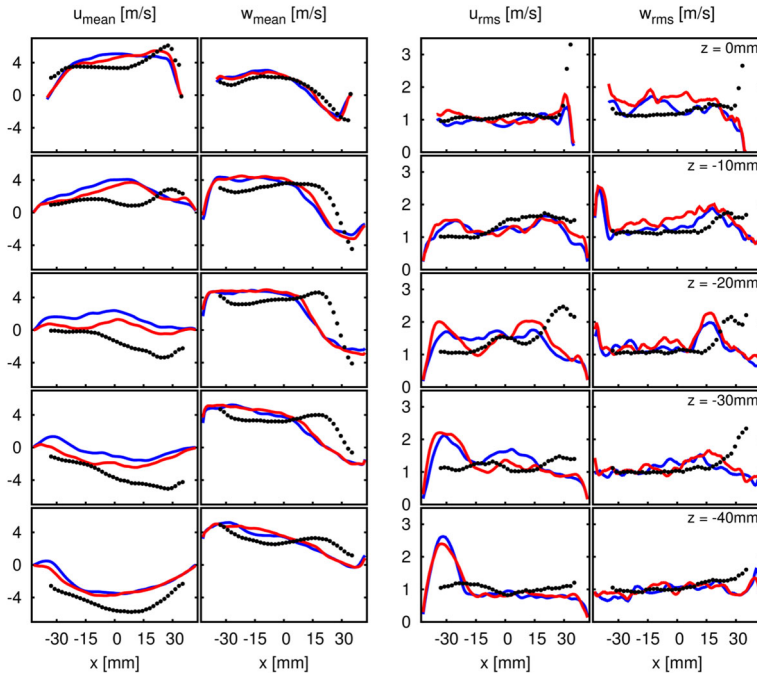


Fig. 12 Phase-averaged velocity profiles and corresponding rms values of velocity components in x -direction during compression at 90° CA bTDC, evaluated at different axial positions (see Fig. 3, right) Comparison between experiments (black points) and LES with a coarse (blue line) and a fine (red line) mesh

The anisotropy distribution shows that during compression at 90° CA bTDC the in-cylinder flow displays a higher tendency towards isotropic turbulence than during intake at 270° CA bTDC. This corresponds to the experimental observations and it can be argued to be due to higher velocities and higher turbulence level associated with the intake stroke. After closing of the intake valves, the in-cylinder flow shows a tendency to *return to isotropy*, as the turbulence decays [37]. Since the movement of the piston head introduces a new disturbance, the in-cylinder flow field is not returning to the state of complete isotropy.

4.3 Sampled investigation of the IC engine flow

A similar analysis to the one performed by Zentgraf et al. [21, 22] concerning the large scale flow phenomena was also conducted on the results of the numerical simulations. Here, the invariants of stationary points within the engine geometry at 270° CA bTDC were extracted and plotted in the AIM together with the Lumley triangle (see Fig. 15). Three zones inside the TPIV measurement domain (black frame) were identified in the experiment. Zone 1 refers to a stagnation line, which is formed between the intake jet and the reverse flow originating from the tumble. The intake jet region is labelled as zone 2 and in zone 3 the change of direction of inlet flow imposed by the cylinder boundaries is considered. For each zone, six data points were extracted and the invariants were calculated. The points belonging to the same zone are marked by colour. This same procedure was used to analyse the numerical results. However, due to the discrepancies between numerical and experimental results, the location of the zones and hence the data points do not correspond identically.

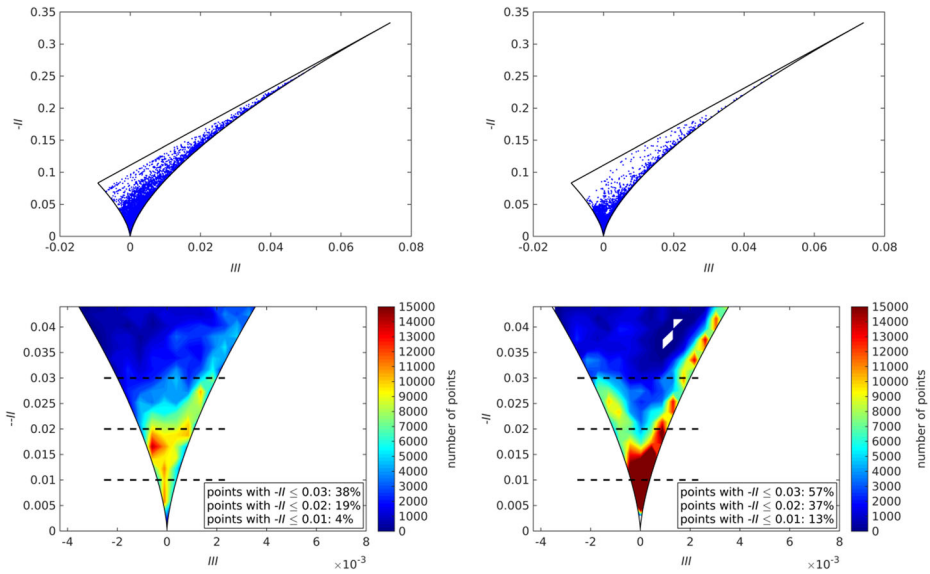


Fig. 13 Scatter plot of points equally distributed in engine cross section at 270° CA bTDC; illustration of numerical data (*left*) and experimental data (*right*) of the whole Lumley triangle (*top*) and an enlarged view of the origin (*bottom*)

As displayed in Fig. 15 the points extracted from zone 1 are mainly located at the right border of the Lumley triangle, which marks the turbulent state of axisymmetric expansion. This implies that one eigenvalue of the anisotropy tensor dominates over the other two and the RST has a prolate shape. Considering the second zone, the data points are located rather at the left boarder of the Lumley triangle, which is characterized by the turbulent state of axisymmetric contraction. Here, two eigenvalues of the anisotropy tensor are dominating over the third one, which is pointing to an oblate shape of the RST. The data points extracted from the third zone shows a tendency towards the origin of the Lumley triangle and therefore to isotropic turbulence. The flow is less anisotropic than in the other zones which means, that the fluctuations do not have any directional preference and the RST has a spherical shape.

4.4 Overall anisotropy behaviour using numerical results

To evaluate the behaviour of the in-cylinder flow field anisotropy during the whole intake and compression stroke, a time-resolved analysis is required. As experimental data are not available at all CA, no comparison has been carried out.

The global behaviour of the anisotropy tensor can be examined using coordinate transformation and averaged invariants plotted against CA. The three dimensional velocity field in the symmetry plane ($y = 0$) (see Fig. 16) was used to calculate the second and third invariant at a certain number of evaluation points. Further, an averaged first and second invariant was calculated every 2 CA for the considered range of 360° – 0° CA bTDC using these evaluation points in the symmetry plane. Since the geometry is changing during the engine cycle, the number of points available for the analysis varies. This analysis should provide indications regarding the overall tendency of the flow field at different states of the engine cycle towards particular turbulence states.

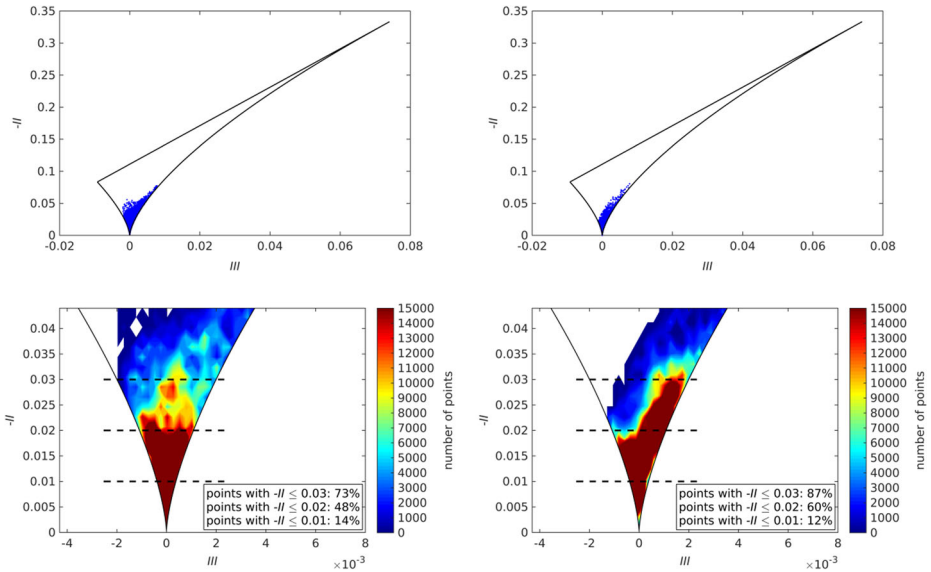


Fig. 14 Scatter plot of points equally distributed in engine cross section at 90° CA bTDC; illustration of numerical data (*left*) and experimental data (*right*) of the whole Lumley triangle (*top*) and an enlarged view of the origin (*bottom*)

Analysing the results in Fig. 16, one can observe an increasing tendency along the state of axisymmetric expansion towards one-component turbulence, starting from 360° CA bTDC. This behaviour is induced by the opening intake valves, where the intake jet is influencing the in-cylinder flow due to high velocities and a strongly directional flow. A fluctuating behaviour can be identified around $300^\circ - 310^\circ$ CA bTDC due to maximum velocity of the intake jet and a high level of turbulence until the averaged invariants computed on the symmetry plane show a tendency towards the origin of the Lumley triangle. After 270° CA bTDC and maximum valve lift at 250° CA bTDC (square mark), the averaged invariants decrease further towards the turbulent state of isotropy until approximately 210° CA bTDC. This is to be expected, as the intake velocity is decreasing and the intake jet loses its influence on the in-cylinder flow. After 210° CA bTDC, the averaged invariants increase again and a trend towards the state of axisymmetric expansion is displayed, which is induced by an increasing intake velocity due to the decreasing area of the intake valve gap. Close to the intake valve closing at 125° CA bTDC (circle mark), the averaged invariants show a fluctuating behaviour again without further tendency towards the isotropic state of turbulence. Instead, starting from approximately 90° CA bTDC they increase: this is probably due to the disturbances of the flow introduced by the piston movement. In this late compression phase towards TDC the so called *vortex breakdown* is taking place, where the rate of decay of the kinetic energy of the mean tumbling motion has been observed to be of the same order of magnitude as its turnover time scale [33, 64]. Here, the kinetic energy is transferred from the large scale tumbling motion to small scale turbulence. According to experimental results of Voising et al. [33], the fluctuating kinetic energy is increasing at the end of compression and at TDC approximately 30% of it is due to cycle-to-cycle variations. This increase can be also detected analysing the behaviour of the anisotropy tensor of the in-cylinder flow.

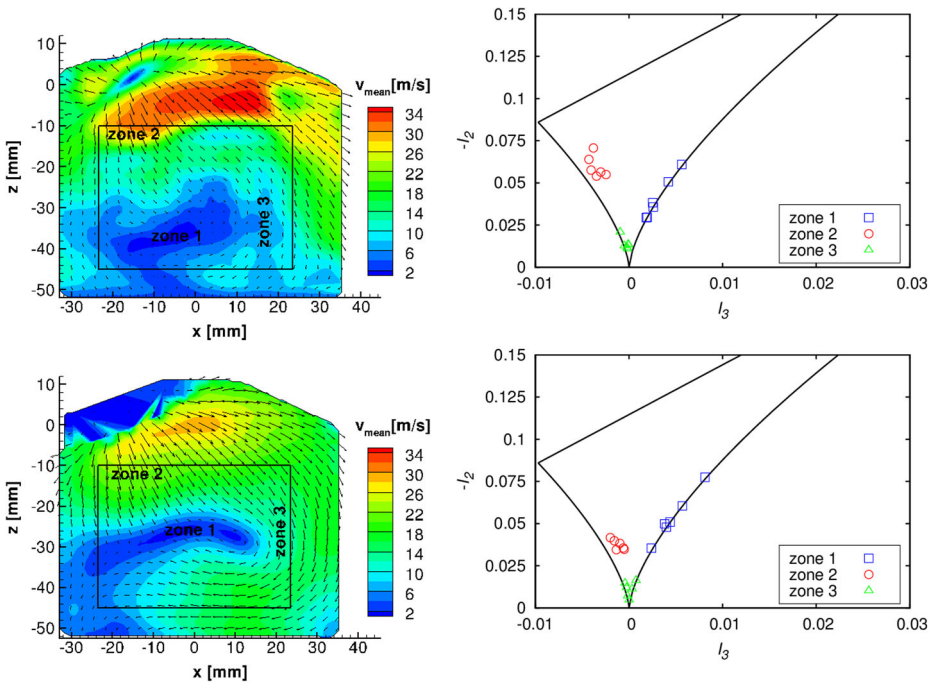


Fig. 15 Points, extracted from different zones of the velocity distribution (*left*) and plotted in the Lumley triangle (*right*) at 270° CA bTDC; top shows numerical and bottom experimental data

The same averaging procedure was performed using a volume instead of the symmetry plain. The representative control volume chosen for the analysis was located at the centre of the cylinder and the invariants were calculated at $78 \times 78 \times 62 = 377208$ points inside of this volume. However, the averaged first and second invariants were calculated only for 270° – 90° CA bTDC (every 2 CA) using these points, since the control volume disappears during the advanced stage of compression. The result is shown in Fig. 17 and one can identify the overall tendency towards isotropy from 270° CA bTDC until 90° CA bTDC as pointed out before. Additionally, the moment of maximum valves lift at 250° CA bTDC (square mark) and the moment of closing the intake valves at 125° CA bTDC (circle mark) are displayed, in a similar fashion as in the previous analysis. Not only the overall tendency towards the state of isotropic turbulence can be observed, but also the increase of the invariants towards the state of axisymmetric expansion corresponding to increasing intake velocity around 210° CA bTDC is reproduced. In general it can be stated, that the results of both averaging procedures illustrated the same tendency of the flow anisotropy.

To illustrate the overall anisotropy evolution without averaging over a large number of points, stationary points on the engine’s symmetry plane ($y = 0$) (see Fig. 3, right) are monitored and reported inside the Lumley triangle (Fig. 18, left). Here, the invariants of the stationary points are plotted every 2 CA and connected by straight lines. The right side of Fig. 18 displays the second and third invariant of the corresponding stationary point (red curves) plotted over CA. As can be seen in both illustrations, the invariants display high levels of fluctuations; this is due to the fact that these quantities depend essentially

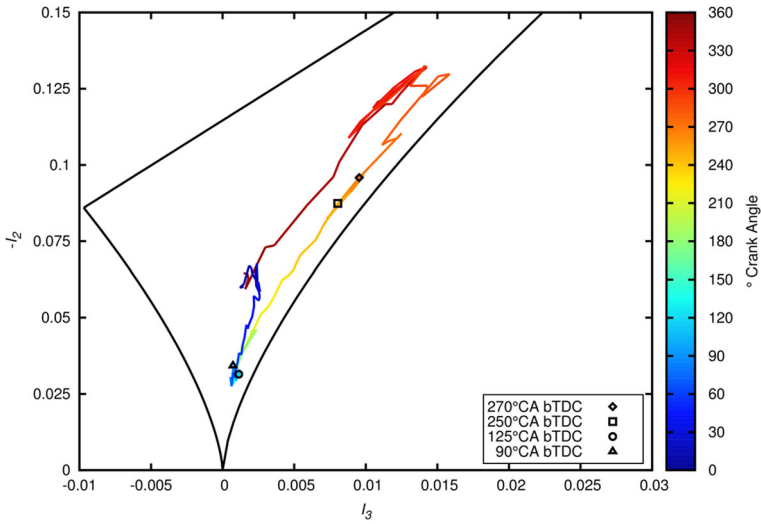


Fig. 16 Averaged invariants on the symmetry plane ($y = 0$) plotted against CA (colour scale) in the Lumley triangle; diamond marks 270° CA bTDC, square marks maximum valve lift at 250° CA bTDC, circle marks intake valve closing at 125° CA bTDC, triangle marks 90° CA bTDC

on the gradients of the velocity field which can vary strongly in time and might require a larger number of cycles to attain a statistically converged value. A smoothing procedure was therefore applied (blue curves) to highlight a statistical trend.

Considering the location of the points inside the engine’s geometry and comparing the overall behaviour of the anisotropy invariants during the whole intake and compression

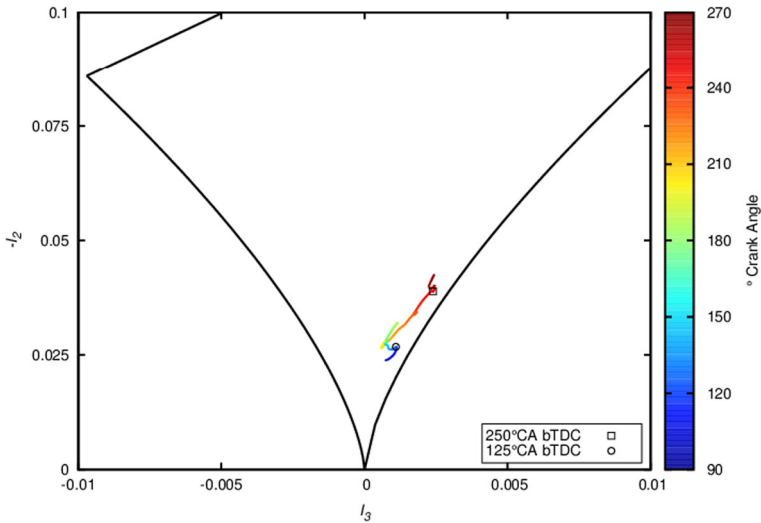


Fig. 17 Volume averaged invariants plotted against CA (colour scale) in the Lumley triangle; volume is located in the centre of the cylinder ($4.8614 \text{ cm} \times 4.8614 \text{ cm} \times 3.8512 \text{ cm} = 91.02 \text{ cm}^3$)

stroke, one can observe decreasing fluctuations and magnitude of the invariants the further away the point is located from the cylinder head and therefore from the intake valves. Additionally, the tendency towards the state of axisymmetric expansion is diminishing and the tendency towards isotropic turbulence is increasing with increasing distance of the points from the cylinder head. This clearly demonstrates the strong influence of the intake jet on the anisotropy of the flow. Considering the temporal evolution of the different stationary points on the other hand, which is indicated by the colour scale in Fig. 18, one can observe a tendency towards the state of axisymmetric turbulence (especially axisymmetric expansion) during the intake stroke and afterwards a tendency towards isotropic turbulence at all points, as previously discussed.

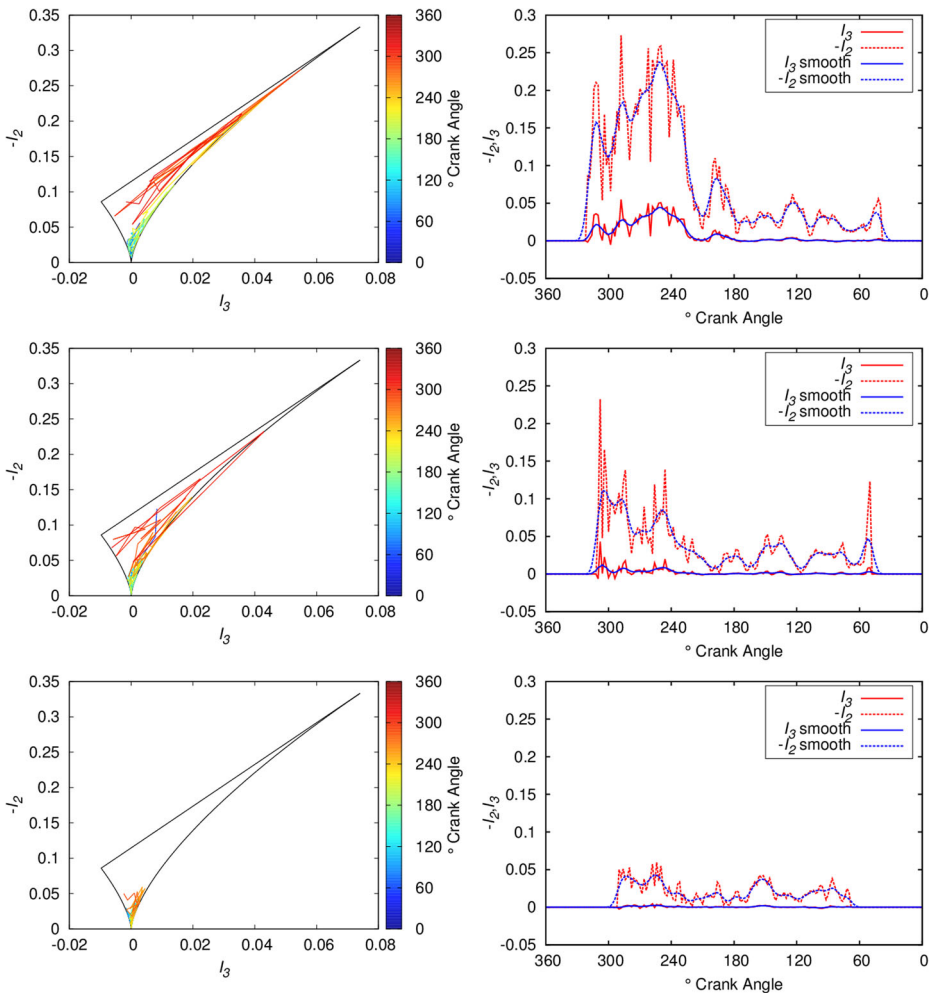


Fig. 18 Evolution of the anisotropy of three stationary points (see Fig. 3, right) plotted against CA (colour scale) in the Lumley triangle (left); first and second invariant (red) and corresponding smoothed curve (blue) plotted against CA (right); top shows first point at $z = -10$ mm, middle second point at $z = -20$ mm and bottom third point at $z = -30$ mm

5 Conclusions

In this work, the velocity field predicted in a motored engine by means of LES was investigated with the objective of characterising it in terms of the anisotropy tensor. Statistical methods were used to obtain information regarding velocity fluctuation during the intake and compression stroke. Based on these, the second and third invariant of the anisotropy tensor were calculated to analyse the turbulent behaviour of the in-cylinder flow.

A comparison of the phase-averaged and rms velocity field with experimental data showed an overall good agreement and considering the restrictions of the application of the Pope [37] quality criterion discussed in Section 4.1, the spatial resolution adopted appears appropriate to describe the turbulent field in most of the computational domain. However, inspection of the M-quality index reveals a clear need for mesh refinement in the region close to the intake valves, where strong velocity gradients are present and are influential for the correct prediction of the tumbling motion. The absence of a specific wall treatment is also likely to affect the predictions, and this point is subject of ongoing investigation. A comparison between experimental and numerical anisotropy distribution at the cylinder symmetry plane as well as a comparison of the turbulent behaviour of large scale flow structures was performed at two different CA. It was found that the large scale structures like the tumble and the intake jet have a strong influence on the anisotropy of the flow. During the intake stroke, the intake jet shows a tendency towards the state of axisymmetric contraction and the stagnation zone located at the centre of the tumble shows a tendency towards the state of axisymmetric expansion. Also, changes of the intake velocity are reflected in the behaviour of the anisotropy tensor.

The time-resolved numerical results provided insight into the flow during the whole engine cycle which cannot be provided by means of experimental investigations alone. The results presented highlighted the highly fluctuating nature of the invariants at stationary points as well as the tendency towards different states of turbulence of the in-cylinder flow at certain times during the intake and compression stroke. Furthermore, the late compression phase was analysed in detail and an increasing tendency towards anisotropy when approaching TDC was observed.

The analysis of the flow anisotropy in IC engines has provided a novel insight in the evolution of the turbulent states realised in different areas of the IC engine and in the overall behaviour of the turbulent flow during the engine cycle as it further lowers the complexity of the data representation.

In the light of the present results it seems possible that a larger number of engine cycles might be needed to obtain statistical convergence in regions of high turbulence intensity, such as the region around the intake valves. It has been shown that the mesh resolution in this area has a strong impact on the prediction of the intake jet as also confirmed by the low value of the Pope quality index adopted in this work. Finally, the analysis of cyclic variations effectively demonstrated in this work has the potential of providing a novel instrument for investigating cyclic variations and their roots in the evolution of the in-cylinder turbulence. The evolution of the anisotropy tensor reflects obviously the break-up and reorganisation of turbulent structure and is indicative of non-local interactions which might be responsible for the amplification of perturbations and ultimately for abnormal events. In which measure the appearance or frequency of strange cycles is affected by the degree of anisotropy found in the turbulence can only be assessed through further simulations and is the subject of ongoing investigations.

Acknowledgements We gratefully acknowledge the financial support of the German Research Council (DFG) through the project SFB/TRR 150. All computations have been performed on the Lichtenberg High Performance Computer at the Technische Universität Darmstadt. Further, the authors would like to thank Andreas Dreizler, Benjamin Böhm, Elias Baum, Florian Zentgraf from Technische Universität Darmstadt, and Brian Peterson from the University of Edinburgh for providing the measurement data as well as for helpful correspondence.

References

- Goryntsev, D.: Large Eddy Simulation of the Flow and Mixing Field in an Internal Combustion Engine. Technische Universität Darmstadt (2007)
- Ghelfi, M.: Large Eddy Simulation in internal combustion Engine. Technische Universität Darmstadt (2013)
- Breitenberger, T.: Numerische Simulation der benzinselbstzündung. Technische Universität Darmstadt (2013)
- Gosman, A.D., Tsui, Y.Y., Vafidis, C.: Flow in a Model Engine with a Shrouded Valve - A Combined Experimental and Computational Study, SAE Tech. Pap., vol. 850498 (1985)
- Le Roy, O., Le Penven, L.: Compression of a turbulent vortex flow. *Int. J. Heat Fluid Flow* **19**, 533–540 (1998)
- Marc, D., Borée, J., Bazile, R., Charnay, G.: Combined PIV and LDV analysis of the evolution and breakdown of a compressed tumbling vortex. In: 11th Symposium on Turbulent Shear Flows (1997)
- Haworth, B.D.C., Jansen, K.: LES on unstructured deforming meshes: towards reciprocating IC engines. In: Proceedings of the 1996 Summer Program, pp. 329–346 (1996)
- Celik, I., Yavuz, I., Smirnov, A.: Large Eddy simulations of in-cylinder turbulence for internal combustion engines: a review. *Int. J. Engine Res.* **2**(2), 119–148 (2001)
- Goryntsev, D., Sadiki, A., Janicka, J.: Analysis of misfire processes in realistic Direct Injection Spark Ignition engine using multi-cycle Large Eddy Simulation. *Proc. Combust. Inst.* **34**(2), 2969–2976 (2013)
- Enaux, B., Granet, V., Vermorel, O., Lacour, C., Thobois, L., Dugué, V., Poinsot, T.: Large eddy simulation of a motored single-cylinder piston engine: Numerical strategies and validation. *Flow Turbul. Combust.* **86**(2), 153–177 (2011)
- Nguyen, T.M., Proch, F., Wlokas, I., Kempf, A.M.: Large Eddy simulation of an internal combustion engine using an efficient immersed boundary technique. *Flow Turbul. Combust.* **97**, 191–230 (2016)
- Nguyen, T., Janas, P., Lucchini, T., D’Errico, G., Kaiser, S., Kempf, A.: LES of Flow Processes in an SI Engine Using Two Approaches: Open Foam and PsiPhi, SAE Tech. Pap., vol. 2014–01–11 (2014)
- Rutland, C.J.: Large-eddy simulations for internal combustion engines - a review. *Int. J. Engine Res.* **12**(5), 421–451 (2011)
- Bottone, F., Kronenburg, A., Gosman, D., Marquis, A.: Large Eddy Simulation of diesel engine in-cylinder flow. *Flow Turbul. Combust.* **88**(1–2), 233–253 (2011)
- Hasse, C., Sohm, V., Durst, B.: Numerical investigation of cyclic variations in gasoline engines using a hybrid URANS/LES modeling approach. *Comput. Fluids* **39**(1), 25–48 (2010)
- Hartmann, F., Buhl, S., Gleiss, F., Barth, P., Schild, M., Kaiser, S.A., Hasse, C.: Spatially Resolved Experimental and Numerical Investigation of the Flow through the Intake Port of an Internal Combustion Engine, *Oil Gas Sci. Technol. - Rev. l’IFP*, vol. 71, no. 2 (2016)
- Borée, J., Miles, P.C.: In-cylinder flow. In: Encyclopedia of Automotive Engineering, pp. 1–31 (2014)
- Spessa, E.: A contribution to the analysis of turbulence anisotropy and nonhomogeneity in an open-chamber diesel engine. *J. Eng. Gas Turbines Power* **121**(2), 226–234 (1999)
- Baum, E., Peterson, B., Surmann, C., Michaelis, D., Böhm, B., Dreizler, A.: Investigation of the 3D flow field in an IC engine using tomographic PIV. *Proc. Combust. Inst.* **34**(2), 2903–2910 (2013)
- Baum, E., Peterson, B., Böhm, B., Dreizler, A.: On the validation of LES applied to internal combustion engine flows: Part 1: Comprehensive experimental database. *Flow Turbul. Combust.* **92**(1), 269–297 (2014)
- Zentgraf, F., Baum, E., Böhm, B., Dreizler, A., Peterson, B.: Analysis of the turbulent in-cylinder flow in an IC engine using tomographic and planar PIV measurements. In: 17th International Symposium on Applications of Laser Techniques to Fluid Mechanics (2014)
- Zentgraf, F., Baum, E., Böhm, B., Dreizler, A., Peterson, B.: On the turbulent flow in piston engines: Coupling of statistical theory quantities and instantaneous turbulence. *Phys. Fluids*, vol. 28 (2016)

23. Vernet, J.: Detailed Study of Steady In-Cylinder Flow and Turbulence using Stereo-PIV. KTH Royal Institute of Technology (2012)
24. Lumley, J.L.: The structure of inhomogeneous turbulence. In: Atmospheric Turbulence and Wave Propagation, Moscow, pp. 166–178 (1967)
25. Borée, J.: Extended proper orthogonal decomposition: a tool to analyse correlated events in turbulent flows. *Exp. Fluids* **35**(2), 188–192 (2003)
26. di Mare, F., Knapstein, R.: Statistical analysis of the flow characteristics and cyclic variability using Proper Orthogonal Decomposition of highly resolved LES in internal combustion engines. *Comput. Fluids* **105**, 101–112 (2014)
27. Böhm, B., di Mare, F., Dreizler, A.: Characterisation of cyclic variability in an optically accessible IC Engine by means of phase-independent POD, LES Intern. *Combust Engines Flows* (2010)
28. Buhl, S., Hartmann, F., Hasse, C.: Identification of Large-Scale Structure Fluctuations in IC Engines using POD-based Conditional Averaging, *Oil Gas Sci. Technol. - Rev. l'IFP*, vol. 71, no. 1 (2016)
29. Lumley, J.L., Newman, G.R.: The return to isotropy of homogeneous turbulence. *J. Fluid Mech.* **82**(1), 161–178 (1977)
30. Lumley, J.L.: Computational modeling of turbulent flows. *Adv. Appl. Mech.* **18**, 123–176 (1978)
31. Lee, M.J., Reynolds, W.C.: Numerical Experiments on the Structure of Homogeneous Turbulence, Tech. Rep. Rep TF-24 (1985)
32. Simonsen, A.J., Krogstad, P.A.: Turbulent Stress Invariant Analysis: Clarification of Existing Terminology. In: 15th Australasian Fluid Mechanics Conference (2004)
33. Voisine, S.M., Thomas, L., Borée, J., Rey, P.: Spatio-temporal structure and cycle to cycle variations of an in-cylinder tumbling flow. *Exp. Fluids* **50**(5), 1393–1407 (2011)
34. Krogstad, P., Torbergsen, L.E.: Invariant analysis of turbulent pipe flow. *Flow Turbul. Combust.* **64**, 161–181 (2000)
35. Uddin, N., Neumann, S.O., Weigand, B.: LES simulations of an impinging jet: On the origin of the second peak in the Nusselt number distribution. *Int. J. Heat Mass Transf.* **57**(1), 356–368 (2013)
36. Nishino, K., Samada, M., Kasuya, K., Torii, K.: Turbulence statistics in the stagnation region of an axisymmetric impinging jet flow. *Int. J. Heat Fluid Flow* **17**(3), 193–201 (1996)
37. Pope, S.B.: *Turbulent Flows*. Cambridge University Press (2000)
38. Radenković, D.R., Burazer, J.M., Novković, D.M.: Anisotropy analysis of turbulent swirl flow. *FME Trans.* **42**(1), 19–25 (2014)
39. Jovičić, N., Breuer, M., Jovanović, J.: Anisotropy-Invariant Mapping of turbulence in a flow past an unswept airfoil at high angle of attack. *J. Fluids Eng.* **128**(3), 559 (2006)
40. Smagorinsky, J.: General circulation experiments with the primitive equations. *Mon. Weather Rev.* **91**(3) (1963)
41. Moin, P., Squires, K., Cabot, W., Lee, S.: A dynamic subgrid-scale model for compressible turbulence and scalar transport. *Phys. Fluids* **3**(1991), 2746–2757 (1991)
42. Banerjee, S., Ertunc, O., Durst, F.: Anisotropy properties of turbulence. In: 13th WSEAS International Conference on Applied Mathematics, pp. 26–57 (2008)
43. Emory, M., Iaccarino, G.: Visualizing turbulence anisotropy in the spatial domain with componentality contours. *Cent. Turbul. Res. Annu. Res. Briefs*, pp. 123–138 (2014)
44. Terentiev, L.: *The Turbulence Closure Model Based on Linear Anisotropy Invariant Analysis*. Universität Erlangen-Nürnberg (2006)
45. Lumley, J.L.: Stochastic tools in turbulence. *Appl. Math. Mech.*, vol. 12 (1970)
46. Choi, K., Lumley, J.L.: The return to isotropy of homogeneous turbulence. *J. Fluid Mech.* **436**, 59–84 (2001)
47. Hamilton, N.M., Cal, R.B.: Characteristic shapes of the normalized Reynolds stress anisotropy tensor in the wakes of wind turbines with counter-rotating rotors. In: 17th International Symposium on Applications of Laser Techniques to Fluid Mechanics (2014)
48. Uruba, V.: (An)isotropy analysis of turbulence. In: *Topical Problems of Fluid Mechanics*, vol. 2, pp. 241–248 (2015)
49. Amsden, A.A., O'Rourke, P.J., Butler, T.D.: *KIVA-II: A Computer Program for Chemically Reactive Flows with Sprays* (1989)
50. Torres, D.J., Trujillo, M.F.: KIVA-4: An unstructured ALE code for compressible gas flow with sprays. *J. Comput. Phys.* **219**(2), 943–975 (2006)
51. Torres, D.J., Li, Y.H., Kong, S.C.: Partitioning strategies for parallel KIVA-4 engine simulations. *Comput. Fluids* **39**(2), 301–309 (2010)
52. ANSYS: *ANSYS ICEM CFD User's manual*, release 15 (2013)
53. di Mare, F., Knapstein, R., Baumann, M.: Application of LES-quality criteria to internal combustion engine flows. *Comput. Fluids* **89**, 200–213 (2014)

54. Baumann, M., Di Mare, F., Janicka, J.: On the validation of large eddy simulation applied to internal combustion engine flows part II: Numerical analysis. *Flow Turbul. Combust.* **92**(2), 299–317 (2014)
55. Heywood, J.B.: *Internal Combustion Engine Fundamentals*. McGraw-Hill, New York (1988)
56. Lumley, J.L.: *Engines - an Introduction*. Cambridge University Press, New York (1999)
57. Catania, A.E., Dongiovanni, C., Mittica, A., Negri, C., Spessa, E.: Turbulence Spectrum Investigation in a DI Diesel Engine with a Reentrant Combustion Bowl and a Helical Inlet Port, SAE Tech. Pap., vol. 962019 (1996)
58. Yoshizawa, A., Horiuti, K.: A Statistically-Derived Subgrid-Scale kinetic energy model for the Large-Eddy simulation of turbulent flows. *J. Phys. Soc. Japan* **54**(8), 2834–2839 (1985)
59. Goryntsev, D., Sadiki, A., Klein, M., Janicka, J.: Large eddy simulation based analysis of the effects of cycle-to-cycle variations on air-fuel mixing in realistic DISI IC-engines. *Proc. Combust. Inst.* **32**(2), 2759–2766 (2009)
60. Fahrmeir, L., Künstler, R., Pigeot, I., Tutz, G.: *Statistik*. 6th edn. Springer Berlin Heidelberg, New York (1997)
61. Buhl, S., Gleiss, F., Köhler, M., Hartmann, F., Messig, D., Brücker, C., Hasse, C.: A combined numerical and experimental study of the 3D tumble structure and piston boundary layer development during the intake stroke of a gasoline engine. *Flow Turbul. Combust.*, pp. 1–22 (2016)
62. Truffin, K., Angelberger, C., Richard, S., Pera, C.: Using Large-Eddy simulation and multivariate analysis to understand the sources of combustion cyclic variability in a spark-ignition engine. *Combust. Flame* **162**(12), 4371–4390 (2015)
63. Granet, V., Vermorel, O., Lacour, C., Enaux, B., Dugué, V., Poinso, T.: Large-Eddy Simulation and experimental study of cycle-to-cycle variations of stable and unstable operating points in a spark ignition engine. *Combust. Flame* **159**(4), 1562–1575 (2012)
64. Borée, J., Maurel, S., Bazile, R.: Disruption of a compressed vortex. *Phys. Fluids* **14**(7), 2543–2556 (2002)